Tectonics

RESEARCH ARTICLE
10.1029/2020TC006628

Key Points:

- We show the first 3-D shallow resistivity image of the M_w 6.5 Norcia earthquake fault system and its main Quaternary hangingwall basin
- The mainshock fault system overprints NNE- and WNW-trending faults that promoted the complex evolution of the Castelluccio hangingwall basin
- We detect two main depocenters, 300 and 500–600 m deep, and a low-angle fault to the south-east of the basin, likely related to thrusting

Supporting Information:

Supporting Information may be found in the online version of this article.

Correspondence to:

F. Villani,
fabio.villani@ingv.it

Citation:

Sapia, V., Villani, F., Fischanger, F., Lupi, M., Baccheschi, P., Pantosti, D., et al. (2021). 3-D deep electrical resistivity tomography of the major basin related to the 2016 M_w 6.5 central Italy earthquake fault. *Tectonics*, *40*, e2020TC006628. https://doi.org/10.1029/2020TC006628

Received 18 NOV 2020
Accepted 19 MAR 2021

Authors Contribution:

Conceptualization: V. Sapia, F. Villani, M. Lupi
Data curation: V. Sapia, F. Villani, F. Fischanger, M. Lupi
Formal analysis: F. Villani, F. Fischanger
Funding acquisition: L. Improta
Investigation: V. Sapia, F. Villani, F. Fischanger, M. Lupi, P. Baccheschi, D. Pantosti, S. Pucci, R. Civico, A. Sciarra, A. Smedile, V. Romano, P. M.

3-D Deep Electrical Resistivity Tomography of the Major Basin Related to the 2016 M_w 6.5 Central Italy Earthquake Fault

V. Sapia[1], F. Villani[1], F. Fischanger[2], M. Lupi[3], P. Baccheschi[1], D. Pantosti[1], S. Pucci[1], R. Civico[1], A. Sciarra[1], A. Smedile[1], V. Romano[4], P. M. De Martini[1], F. Murgia[4], V. Materni[1], F. Giannattasio[1], L. Pizzimenti[5], T. Ricci[1], C. A. Brunori[1], I. Coco[1], and L. Improta[1]

[1]Istituto Nazionale di Geofisica e Vulcanologia, Rome, Italy, [2]Geostudi Astier, Livorno, Italy, [3]Department of Earth and Environmental Sciences, University of Geneva, Geneva, Switzerland, [4]Department of Earth Sciences, University La Sapienza, Rome, Italy, [5]Soft Strategy Group S.p.A., Rome, Italy

Abstract We provide the first 3-D resistivity image of the Pian Grande di Castelluccio basin, the main Quaternary depocenter in the hangingwall of the Mt.Vettore–Mt. Bove normal fault system (VBFS), responsible for the October 30, 2016 M_w 6.5 Norcia earthquake (central Italy). The subsurface structure of the basin is poorly known, and its relation with the VBFS remains debated. Using the recent Fullwaver technology, we carried out a high-resolution 2-D transect crossing the 2016 coseismic ruptures coupled with an extensive 3-D survey with the aim of: (a) mapping the subsurface of the basin-bounding splays of the VBFS and the downdip extent of intrabasin faults; (b) imaging the infill and pre-Quaternary substratum down to ~1 km depth. The 2-D resistivity section highlights under the coseismic ruptures a main dip-slip fault zone with conjugated splays. The 3-D resistivity model suggests that the basin consists of two depocenters (~300 and ~600 m deep, respectively) filled with silty sands and gravels (resistivity <300 Ωm), bounded and cross-cut by NNE-, WNW-, and NNW-trending faults with throws of ~200–400 m. We hypothesize that the NNE-trending system acted during the early basin development, followed by NNW-trending and currently active splays of the VBFS that overprint pre-existing structures and locally control the infill architecture. Moreover, beneath the basin we detect a shallow NW-dipping blind fault. The latter is likely a hangingwall splay of the adjacent regional Mts. Sibillini Thrust, which may have been partly involved in the rupture process of the Norcia mainshock.

1. Introduction

Fault-related extensional basins often display complex subsurface architecture with numerous cross-cutting geological features that derive from multiphase tectonics (Civico, Sapia, et al., 2017, Meghraoui et al., 2000; Reeve et al., 2015, and references therein). The mechanical response of the upper crust and permanent displacement of the topographic surface due to long-term normal faulting control the hangingwall basin size, depth, and shape. Moreover, these processes affect the erosional and depositional systems that eventually reflect in the sedimentary basin record (Burbank & Anderson, 2011; Gawthorpe & Leeder, 2000). Therefore, understanding the subsurface geometry and architecture of the basins, through geophysical imaging, is of utmost importance to reconstruct long-term (10^5–10^6 yr timescales) fault activity and evolution of crustal seismogenic normal faults.

The Neogene central Apennines fold-and-thrust belt (Italy) is a region of Pliocene-Quaternary extension overprinting a previously shortened crust (Boncio et al., 2004; Boncio & Lavecchia, 2000; Cowie & Roberts, 2001; Lavecchia et al., 1994; Tondi, 2000) through a network of NW-trending normal faults (Galadini & Galli, 2000). Normal faulting is responsible for the bulk of the current seismic release (Chiarabba et al., 2005; Cowie et al., 2017) with damaging events characterized by magnitude M6+, generally causing surface faulting (Galli, Galadini, & Pantosti, 2008). The October 30, 2016, M_w 6.5 Norcia normal-faulting earthquake, the strongest shock of the 2016–2017 central Italy destructive sequence (named Amatrice, Visso, and Norcia earthquake sequence; Figure 1a; Chiaraluce et al., 2017), is the best documented example of a complex multi-segment rupture event in the Apennines extensional belt (Improta, Latorre, et al., 2019; Scognamiglio et al., 2018; Walters et al., 2018). This event ruptured two main NNW-trending

De Martini, F. Murgia, V. Materni, F. Giannattasio, L. Pizzimenti, T. Ricci, C. A. Brunori, I. Coco, L. Improta
Methodology: F. Fischanger
Project Administration: L. Improta
Resources: F. Fischanger, M. Lupi
Software: F. Fischanger
Supervision: V. Sapia, M. Lupi
Validation: V. Sapia, F. Villani, F. Fischanger
Visualization: F. Villani, P. Baccheschi
Writing – original draft: V. Sapia, F. Villani, F. Fischanger, M. Lupi, P. Baccheschi, L. Improta
Writing – review & editing: V. Sapia, F. Villani, F. Fischanger, M. Lupi, P. Baccheschi, D. Pantosti, S. Pucci, P. M. De Martini, L. Improta

and WSW-dipping Quaternary normal fault systems: the Mt. Vettore–Mt. Bove normal fault system (VBFS) to the North, and the northern part of the Laga Mts. fault system to the South for a total length of about 35 km (Figure 1a; Pizzi et al., 2017). The fault segmentation is controlled by an NNE-trending and gently dipping transverse structure (likely inherited from Neogene compressional tectonics), which influenced the coseismic slip propagation and, in turn, ruptured during the mainshock releasing ~30% of total seismic moment (Figure 1b; Scognamiglio et al., 2018). Large part of the seismic moment was released by a main, <6 km-deep slip patch that relates to the VBFS, and induced a >22-km-long surface rupture with average slip of 0.45 m and local peaks >2 m (Brozzetti et al., 2019; Villani, Pucci, et al., 2018). The exposed coseismic fault scarps mostly affect bedrock carbonates, but surface faulting also affected the northern part of the Pian Grande di Castelluccio basin (hereinafter PGC; e.g., Villani, Sapia, et al., 2019), which represents the main Quaternary tectonic depression in the hangingwall of the VBFS (Figure 1). The geological setting of this region has been the object of several works in the past three decades (e.g., Boncio et al., 2004; Calamita, Pizzi, & Roscioni, 1992; Galadini & Galli, 2003; Pierantoni et al., 2013), and its seismotectonic framework has been extensively investigated through geological and paleoseismological studies after the 2016 mainshocks (Cinti et al., 2019; Galli, Galderisi, et al., 2019). These studies suffer from a poor knowledge of the relationships between surface and subsurface structures, due to the lack of good quality seismic exploration data. The latter is indeed limited to a regional section merging three commercial profiles (acquired in the '80s) of fair to low resolution that crosses the epicentral area in correspondence of the PGC basin (Porreca,

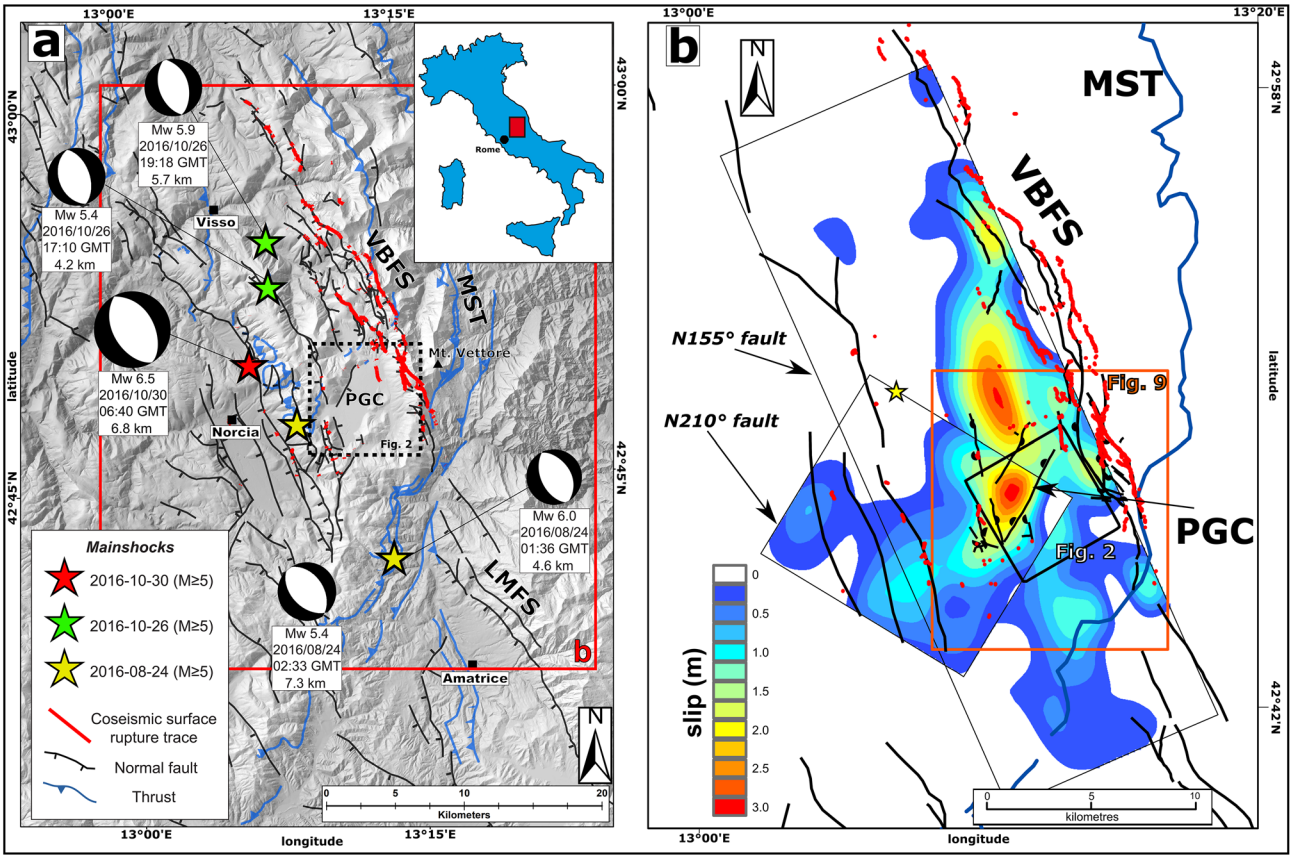

Figure 1. Seismotectonic and geological setting of the survey area. (a) Structural setting of the central Apennines with main Quaternary normal faults (solid black lines; VBFS, Vettore–Bove fault system; LMFS, Laga Mts fault system), thrusts (solid blue lines; MST, Mt. Sibillini Thrust), surface faulting of the Amatrice, Visso, and Norcia earthquake sequence (solid red lines, modified after Civico, Pucci, et al., 2018), and the focal mechanisms of the mainshocks (http://terremoti.ingv.it/tdmt; hypocentral depths after Improta, Latorre, et al., 2019); the red rectangle indicates the area of panel (b), and the black dashed box indicates the area shown in Figure 2. (b) Slip model of the M_w 6.5 Norcia earthquake (modified after: Scognamiglio et al., 2018): the two gray boxes represent the projection of the main modeled fault planes (top of 155°N fault is located at 850 m a.s.l; top of 210°N fault is located 1,000 m below sea level), black lines are normal faults, blue lines are thrusts, red lines are coseismic surface ruptures, the black square indicates the extent of the Fullwaver (FW) survey area (shown in Figure 2), and the orange box indicates the extent of Figure 9 (PGC, Pian Grande di Castelluccio basin). Geographic coordinates, WGS84 reference datum, zone 33N.

Minelli, et al., 2018). The VBFS and the PGC basins are barely visible in this seismic section, thereby the fault geometry at depth, as well as its structural relationships with Mio-Pliocene contractional structures of the Apennines thrust belt, remains uncertain. Additionally, high-resolution aftershocks catalogs provide high-quality pictures of the fault systems activated during the sequence at depths >3–4 km (Improta, Latorre, et al., 2019; Michele et al., 2020).

From previous considerations, it follows that the PGC basin is a primary target to improve the knowledge of the VBFS through an accurate 3-D reconstruction of its geometry and internal structure, which may provide insights into the long-term evolution, interaction, and segmentation of the complex system of faults that bounds the basin. Indeed, the genesis and evolution of the PGC can be hardly ascribed only to the activity of the Mt. Vettore fault: the rhomboidal basin shape (Figure 1b) suggests a complex interplay of NNW-trending structures and oblique faults (Villani, Sapia, et al., 2019). The model of rhomb-shaped basin controlled by oblique faults has been proposed in the finite-fault inversion of the M_w 6.5 Norcia mainshock by Walters et al. (2018) to infer the geometry of a subsidiary, blind oblique fault segment activated at the eastern edge of the PGC (namely, Pian Piccolo fault).

In spite of multidisciplinary shallow geophysical surveys carried out after the 2016–2017 seismic sequence (Villani, Sapia, et al., 2019), large uncertainties still remain about the three-dimensional structure of the PGC basin. The integration of H/V ambient noise measurements and time domain electromagnetic soundings (TDEM) with 2-D shallow electrical resistivity tomography (ERT), points out an asymmetric graben structure up to 300 m deep and dissected by several fault splays. However, the recovered subsurface images, intrinsically limited on the interpolation of 1-D and 2-D surveys (Haining et al., 2010), provide only inferences on the true 3-D basin structure (details in supporting information S1) (Sapia et al., 2014, 2015).

To accurately image complex intramontane basins, a fully 3-D exploration strategy combining a high spatial resolution with adequate investigation depth is needed (Butler, 2005; Paul, 2015; Pugin et al., 2014; Schamper et al., 2014; Viezzoli et al., 2013; Everett, 2013). Although seismic reflection is typically the most effective approach to image tectonic structures, a high-resolution 3-D seismic survey of the whole PGC basin is not feasible due to prohibitive cost, logistic difficulties, and high-environmental impact (the PGC is located in a natural park) (Telford et al., 1990; Yilmaz, 2001). As an alternative, we used the innovative Fullwaver (FW) system that can be used to perform shallow and deep ERT. Following 3-D survey strategies, this system can acquire a large number of subsurface data in a relatively short time (Gance et al., 2018). Thanks to its flexibility that allows it to tackle challenging logistics, this cost-effective technology has been successfully applied to map 3-D aquifer geometry and shallow geothermal fields in an urbanized setting (Carrier et al., 2019). It has also been used to survey large-scale hydrogeological and volcanic structures in areas characterized by slope instability (Lajaunie et al., 2019), and dense urbanization (Troiano et al., 2019).

In May 2019, we carried out an FW geoelectrical survey following a multiscale exploration strategy. A 3-D survey covering almost the entire PGC basin, was first designed with an adequate compromise between spatial resolution and investigation depth. Next, it was complemented by a 2-D high resolution transect in the northern sector of the basin (Figure 2).

In particular, the 3-D survey covered a ~40 km^2 area and was designed to map the whole basin structure taking into account the rugged topography and local logistics. The 2-D transect, 1.4 km long, was purposely centered onto the fault splay of the VBFS that ruptured the surface during the M_w 6.5 2016 mainshock (labeled as Valle delle Fonti Fault [VF]; Villani & Sapia, 2017). To our knowledge, this is the first application of this innovative geoelectrical method to investigate the 3-D structure of a large basin related to a major seismogenic fault system.

This multiscale survey aims at: (1) producing a 3-D resistivity model of the entire basin down to a depth of ~1 km b.g.l.; (2) mapping the geometry of the pre-Quaternary carbonatic substratum and the basin infill; (3) imaging the subsurface of known faults below the plain; (4) defining the subsurface geometry and the internal resistivity structure of the fault zone associated with coseismic surface ruptures; and (5) mapping possible unknown blind fault splays and understanding their relations with the VBFS.

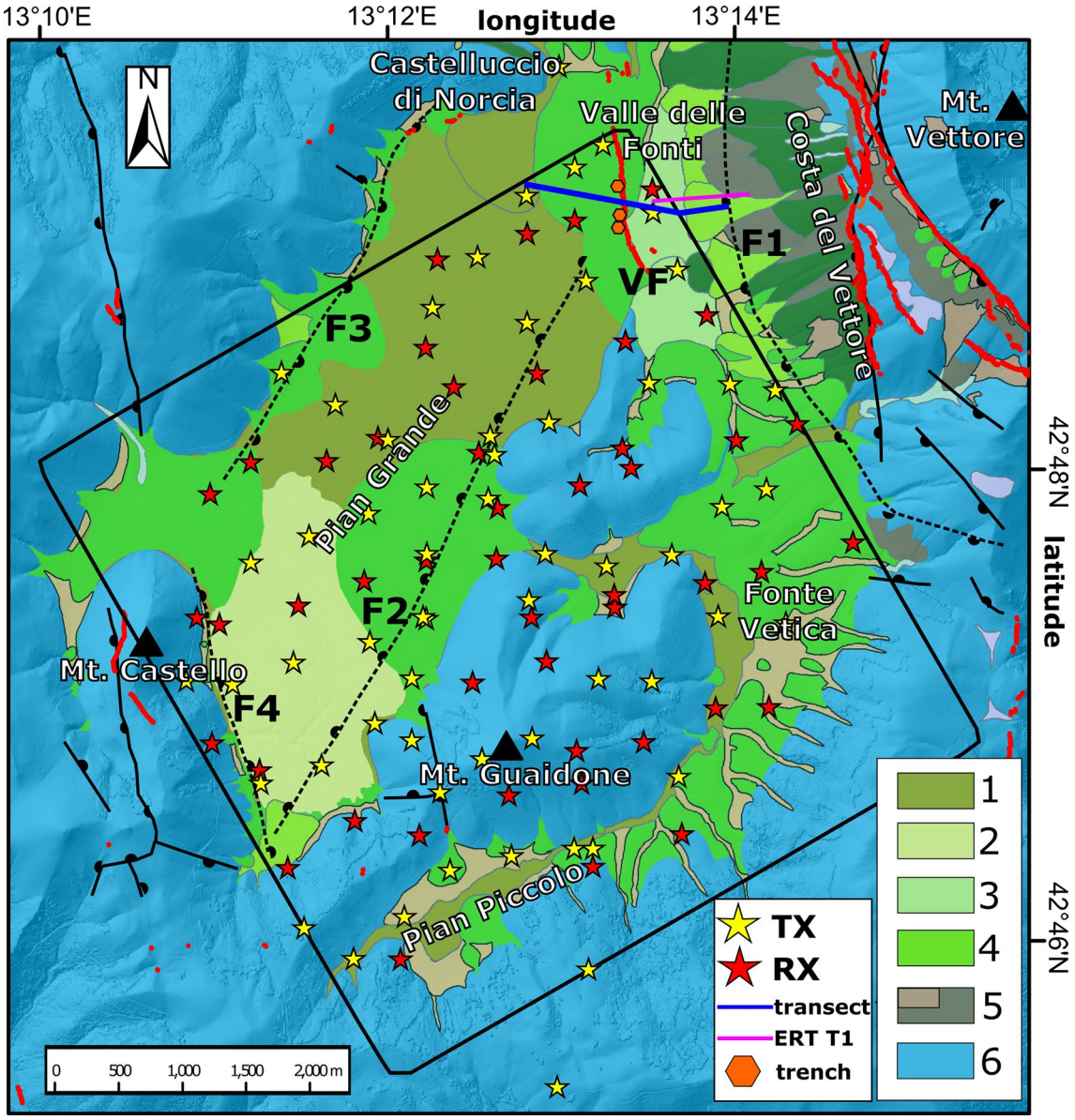

Figure 2. Geology of the PGC basin area (simplified after: Pierantoni et al., 2013). Solid black lines are faults (faults F1–F4 after Villani, Sapia, et al., 2019), red lines are the 2016 surface ruptures, small orange symbols indicate paleoseismic trenches by Galadini and Galli (2003) across the Valle delle Fonti fault. Yellow and red stars locate the Fullwaver survey TX and RX positions, respectively. The blue line indicates the trace of the 2-D transect, the pink line indicates the trace of ERT T1 by Villani, Sapia, et al. (2019). The black square encloses the 3-D resistivity grid. Key to legend: (1) recent distal alluvial fan sediments; (2) recent palustrine sediments; (3) alluvial fan (Late Pleistocene-Holocene); (4) alluvial fan (Middle Pleistocene-Holocene; (5) scree and debris flow (Late Pleistocene-Holocene); and (6) undifferentiated pre-Quaternary bedrock (limestones, cherts, and marls; Early Jurassic to Eocene). Geographic coordinates, WGS84 reference datum, zone 33N. Shaded-relief topography from Tarquini et al., 2012.

2. Materials and Methods

The survey area enclosed a large part of the PGC basin and lowermost fault splays of the VBFS. Prohibitive environmental and topographic conditions hamper the investigation of the highest active splays cross-cutting the Mt. Vettore ridge crest at >1,800–2,000 m a.s.l. (Figure 2). We used 24 independent 2-channels digital receivers to record the electrical field generated by a 5 kW time-domain induced polarization transmitter through several current injections. The FW acquisition scheme is similar to the measurement principle adopted for any multielectrode resistivity meters. A current is injected into the ground through an induced polarization transmitter (TX) using two electrodes (AB) and the resulting voltage is

captured by two other receiver electrodes (MN), thus forming a quadrupole measurement. Input current is recorded in real time and the entire set of transmitters and receiver boxes (RX) are global navigation satellite system synchronized. We injected from 2 to 4 A during an acquisition window of ~240–300 s to obtain as many stacks as possible in order to increase the signal-to-noise ratio. We carried out two distinct surveys: (a) a high-resolution 2-D transect, 1.4 km long, was measured deploying the 24 FW receivers (V-FW) with a constant spacing of 15 m between receiver and transmitter dipole electrodes; (b) a 3-D grid was arranged according to logistics and topography to cover an area of about 40 km^2. Due to the available V-FW, the basin was divided into two subareas, the western and eastern one, respectively, which were measured separately by means of 25 current injections. As for the 3-D survey, receiver dipole length was set to 200 m and the spacing between each V-FW was set to an average distance of 450 m, variable according to logistics (e.g., roads, field borders, and steep slopes). Each dipolar transmission was then set within the 3-D grid and aligned along almost parallel paths for a total of 50 transmissions (Figure 2). To optimize the design of the 3-D survey, we preliminarly performed a synthetic analysis to check the expected level of the signal at each receiver for all transmissions down to a depth of ~1.5 km (details in supporting information S2).

The processing workflow included the following main steps: (i) filtering spikes and self-potential jumps, (ii) computing the average voltage resulting from a current injected on the stacked period, and (iii) calculating the resistance from the previous measurements (more details in supporting information S3). The inverted 3-D data set consisted of 2,448 quadrupoles while the 2-D transect is composed of 1,392 quadrupoles. In general, we injected between 1 and 3.5 A depending on TX dipole sizes and ground resistance (the higher the TX size and the ground resistance the lower was the injected current). This approach, combined with a general high background resistivity of the site, in most of the cases allowed recording high potentials at the receivers, with average and median amplitudes of 15 and 5 mV, respectively. In terms of measured apparent resistivity, the average and median values are 320 and 307 Ωm for the 2-D survey and 500 and 415 Ωm for the 3-D survey, respectively. For the 3-D survey, negative values of apparent resistivity were recorded as the result of peculiar combinations of TX/RX electrodes and due to the RX dipole size and their arrangement over areas of strong horizontal resistivity variation (locally implying changes from 100 to >5,000 Ωm). These data were included in the inversion. Processed data were modeled via a regularized inversion with smoothness constraints (supporting information S4) to cope with the expected strong subsurface resistivity changes and to obtain robust 2-D and 3-D resistivity models, respectively.

Forward modeling was performed through a finite element (FE) approach, in which the region is discretized into a mesh of tetrahedral elements with an assigned resistivity value, and an approximate solution is determined at each node (more details in supporting information S4).

We inverted the 2-D and the 3-D survey data sets separately. In fact, the transect aimed at obtaining a high-resolution image of the shallow subsurface structure of the 2016 coseismic ruptures. Conversely, the 3-D survey targeted a much wider area and the deeper structure of the basin, at the expense of a loss in spatial resolution. To this end, we purposely adopted two different survey strategies, with different resolutions and depth of investigation.

For the 2-D transect, we built a high-resolution mesh (5 × 5 × 5 m) with a foreground depth of 300 m. We parameterized the inversion using a starting model of 500 Ωm and "isotropic" roughness $x = 1$, $y = 1$, and $z = 1$. The starting resistivity model is based on the evidence of low-to-medium resistivity outcropping alluvial sediments. The estimated noise on the data was set to be equal to 0.5% for V/I ratio measurements. The theoretical maximum investigation depth (1,200 m) was estimated, first, by integrating the analytic sensitivity function—for the larger TX/RX combinations—and then by calculating the median z depth, so that the area under the sensitivity curve is equal to 50% of the total area (Barker, 1991). As for the 3-D inversion, we started from a homogeneous reference model of 1,000 Ωm, which better represents the general background of the area, characterized by widespread outcrops of carbonate rocks. We build an FE 3-D mesh (50 × 50 × 50 m) and 1,200 m foreground depth. We imposed an anisotropic roughness scheme $x = 1$, $y = 1$, and $z = 0.01$ to highlight strong resistivity changes expected at the interface between basin infill and the carbonate substratum. We also carried out an inversion with an isotropic scheme, with very subtle differences in the output resistivity model (Figures S4 and S5). The estimated data noise was set to 1% for V/I measurements.

3. Results

3.1. Resolution Limits, Uncertainties, and Interpretation Strategy

Sensitivity is a reasonable quantity to interpret the resolution capability of a given resistivity data set. Indeed, the sensitivity function captures the changes in the potential due to changes in resistivity of a cell volume (Okpoli, 2013). We have performed a thorough sensitivity analysis (see details in supporting information S5), using the normalized sensitivity function to assess the resolution depth of our 3-D resistivity model. In this case, we assume that the 3% of the maximum normalized sensitivity value is a good indicator for the resolution depth. The resolved regions of the models in the central part of the surveyed region are as deep as 700–800 m b.g.l. Beside intrinsic method limitations (i.e., spatial resolution, loss of sensitivity with depth, supporting information S5) and geological factors (nonunique relationship between lithology and resistivity, also influenced by rock fracturing and fluid content), we recognize spatially persistent features with well-defined resistivity contrasts. Moreover, the spatial resolution set a lower bound for the smallest and shallowest resolvable structures (in the order of ∼50 m) and for geological features characterized by a weak electrical resistivity contrast. Nonetheless, the obtained 3-D model represents a good compromise between extent and depth of the scientific targets (i.e., basin and fault imaging), available instrumentation, logistical issues, spatial resolution, and investigation depth.

The choice of 200 m receiver dipole length is justified by the need to cover the entire survey area with the available 24 V-FW while preserving an acceptable signal-to-noise ratio at each receiver, and thus to properly image both shallow and deep targets. However, the combination of sparse sets of receivers paired with a limited number of current injections, mainly affected our capability to resolve the shallower 50 m of the subsurface, which may result in inadequately recovering the small-scale near-surface heterogeneities. Moreover, the substratum consists of a multilayer of limestones with variable fracturing and/or marly content. Nonetheless, their resistivity response remains generally high, thus making any internal lithological layering undetectable.

We are aware that changes in resistivity also result from variation in fluid content and type. Thus, in the absence of quantitative data on local aquifers, we assume that groundwater resistivity within the investigated volume is nearly constant. Nevertheless, channelized fluid flow into fault zones possibly enhanced subvertical electrical resistivity contrasts and thus our capability to depict tectonic lineaments.

3.2. Resistivity-Lithology Association

The PGC basin is emplaced on Jurassic-Eocene massive limestones and thin-bedded marly limestones and cherts of the Umbria-Marche sequence (Pierantoni et al., 2013), stacked during the Miocene by regional NNW-trending thrusts (in particular, the Mt. Sibillini Thrust [MST] in Figure 1a). These rocks, exposed along the basin-bounding ridges (Figure 2), are covered by Middle Pleistocene to Holocene alluvial fans and fluvioglacial deposits of unknown thickness (Coltorti & Farabollini, 1995). Some shallow boreholes (<100 m deep; Ge.Mi.Na., 1963) penetrate alternations of gravels, sandy gravels, and clays and provide only sparse constraints on very shallow resistivity contrasts (Villani & Sapia, 2017).

We first defined a general association between resistivity values of the 3-D model and lithology based on the results of previous shallow ERT surveys of the PGC basin (Villani & Sapia, 2017). We also use results of shallow to deep ERT surveys carried out in similar intramontane basins of the Apennines (Giocoli et al., 2011; Pucci, Civico, et al., 2016; Villani, Tulliani, et al., 2015). These studies indicate that fluviolacustrine silty sands and gravels generally show low resistivity (ρ ∼20–200 Ωm), whereas marly to massive limestones exhibit higher resistivity (ρ from 700 to >2,000 Ωm). Intermediate values of resistivity are typical of coarse-grained deposits, with alluvial fan conglomerates and slope breccias (ρ ∼800 Ωm; Colella et al., 2004; Balasco et al., 2011). Such values are comparable to those of fractured and/or weathered limestones, therefore mapping the substratum of the PGC can be difficult because it is locally covered by thick coarse deposits. To overcome this ambiguity, we corroborate our interpretations with TDEM soundings and ambient noise measurements providing consistent indications on the limestone substratum depth for numerous sites of the basin (Villani, Sapia, et al., 2019).

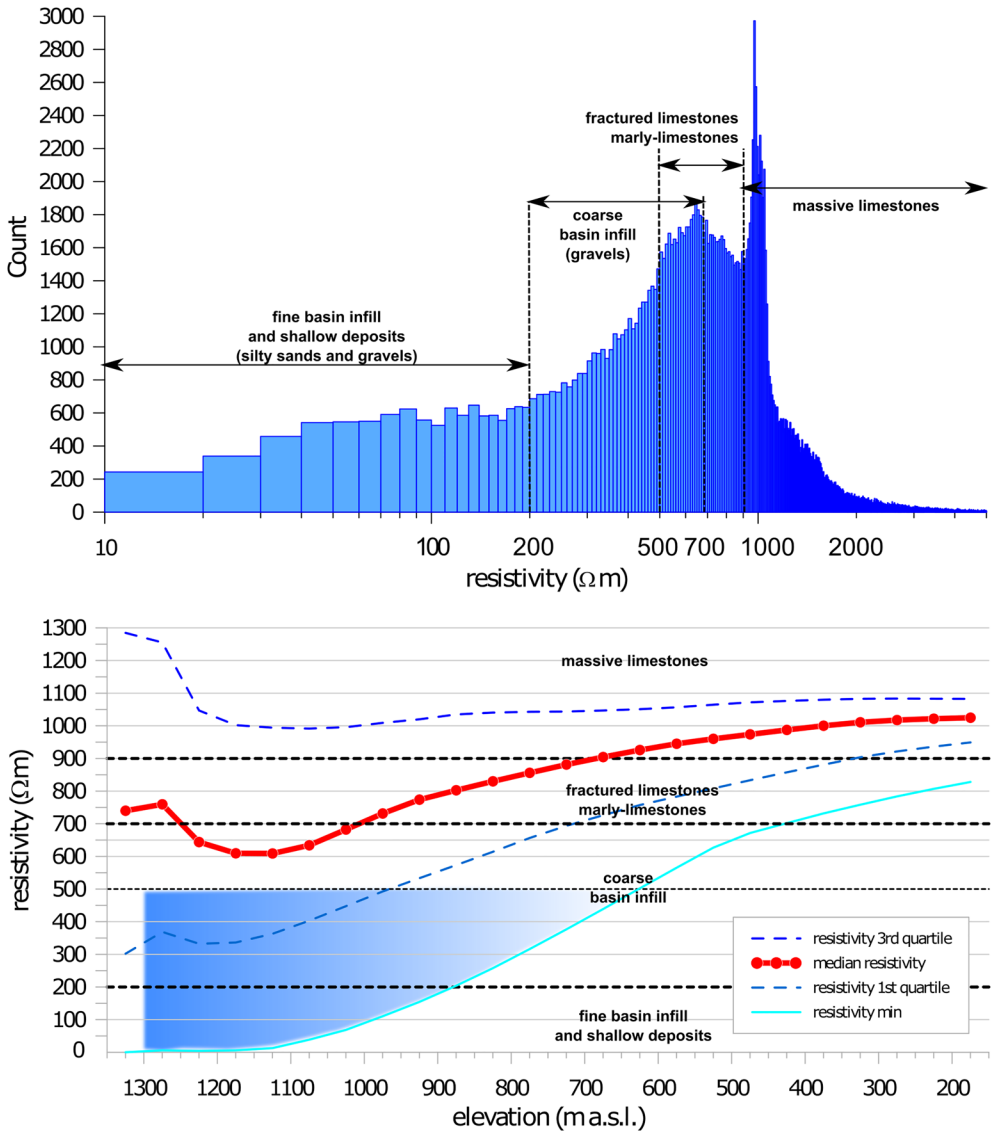

Figure 3. Resistivity classification of the Fullwaver model based on statistical analysis. Top: frequency histogram of resistivity values from the 3-D model (logarithmic *x*-axis; bin size 10 Ωm); the vertical dashed lines indicate classification boundaries of the main electrical units (double arrows show the approximate resistivity range for each unit; some overlap exists for coarse infill and fractured marly limestone). Bottom: statistical parameters of resistivity versus elevation (minimum value, first interquartile, median, and third interquartile) extracted from 24 layers spaced 50 m apart along the *z*-direction; the blue-shaded area indicates the inferred contribution from the PGC basin infill material.

Figure 3 shows the frequency distribution of the resistivity values of the 3-D model and the inferred association between resistivity and lithology. Neglecting the 1,000 Ωm peak (related to unresolved and/or unperturbed regions of the model), the basin substratum is highly resistive (>2,000 Ωm), despite the relatively shallow depth and the intense deformation of the carbonate multilayer.

The distribution of the resistivity values versus depth is shown in Figure 3 (bottom panel). The range of resistivity is inversely related to depth. The large variability and heterogeneity down to ~500 m depth, where the sensitivity is higher, is mostly due to the basin infill material (blue-shaded area in Figure 3).

We therefore adopt the following classification. For the basin infill, silty sands of distal alluvial fan and lacustrine facies represent the low resistivity structures ($\rho \leq 200$ Ωm) while gravels exhibit moderate-to-high resistivity ($\rho \sim 200–500$ Ωm). In addition, relatively high resistivity (up to $\rho \sim 700–800$ Ωm) can be related to

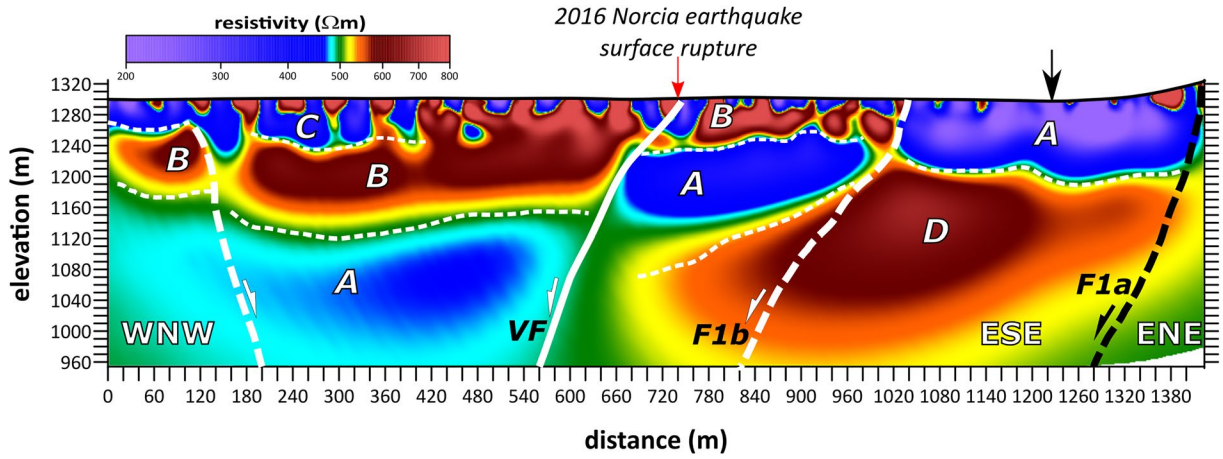

Figure 4. High-resolution 2-D Fullwaver resistivity section (blue line in Figure 2) across the October 30, 2016 surface ruptures and trenches by Galadini and Galli (2003) (location in Figure 2). No vertical exaggeration. The black arrow at x = 1,220 m indicates the point of strike change of the survey line (see Figure 2). Thick and dashed white lines delineate normal fault splays as inferred by lateral resistivity variations; black dashed line indicates F1a that is one of the fault splays belonging to the VBFS inferred by Villani, Sapia, et al., 2019 on the basis of previous geophysical investigations; thin dashed white lines highlight the main electrical units A, B, C, and D described in the text. The logarithmic color scale (different from the one used in Figures 5–7) is histogram-equalized to enhance subtle resistivity changes.

more proximal alluvial fans and slope carbonate clastics. The substratum displays a wide range of resistivity: low values (ρ ~500–1,000 Ωm) can be associated to fractured limestone within fault zones and to marly limestone, whereas resistivity ρ >1,000 Ωm can be related to massive limestones (Figure 3). We remark that such a general resistivity-lithology association aims at interpreting the first-order features of the 3-D resistivity model.

3.3. 2-D Transect Results

The resistivity model of the 2-D transect is shown in Figure 4. During the survey, we performed four additional external transmissions on the western slope of Mt. Vettore (Coste del Vettore, Figure 2) up to 1,530 m a.s.l. (>200 m above the survey line) for deeper current penetration. We interpret only the uppermost 300 m of the section, since the 2-D model is resolved down to about ~1,000 m a.s.l.

The shallow part is characterized by a moderately resistive region to the East (ρ ~200–350 Ωm). This body (unit A) is overlaid by a high-resistivity region (ρ ~500–600 Ωm) ~50 m thick at x = 780–1,000 m, and ~90 m thick at x = 180–660 m (unit B). A thin moderately resistive body (unit C) occurs in the shallower portion at x = 0–360 m. The deep part of the model is partitioned into two regions: a high resistivity region to the East (up to ρ ~800 Ωm) and a moderately resistive region to the West (ρ ~300–470 Ωm), separated by a strong lateral variation at about x = 650 m. We interpret the shallow bodies, together with unit A, as thick layers of gravels and sands, with subordinate patches of silts that promote a local lowering of resistivity. The geometry of these electrical layers can be ascribed to at least three different stacked alluvial fans (A, B, and C). Conversely, the eastern deep, high resistivity body (unit D) can be related either to a marly-limestone substratum or to coarser and likely cemented fan deposits. We suggest that unit D may include both geologic units. The nearby high-resolution ERT T1 of Villani, Sapia, et al. (2019), extending 300 m eastward onto the ridge slope (trace in Figure 2), indicates the occurrence of coarse-grained slope deposits showing similar resistivity (ρ >750–800 Ωm), partly explained by the presence of limestone boulders. However, the large thickness of the eastern body (>250 m) better reconciles with slope and fan coarse deposits.

Overall, the geometry of units A and B together with their thickness changes, highlights the presence of two main normal fault splays (VF and F1b, Figure 4) belonging to the VBFS and distributed in a fault zone 300–400 m wide. In addition, in the western part, a subtle vertical displacement of unit B suggests the presence of a small antithetic normal fault dipping to the East (at x = 180 m), with an associated throw of about 40–60 m that promoted deposition of unit C. The splay labeled as VF matches the 2016 Norcia earthquake surface rupture, and is characterized by a high-angle geometry. This fault zone corresponds to the mapped

fault VF at the surface (Figure 2). Syn-sedimentary fault activity is evidenced by thickening of units A and B in the fault hangingwall. The cumulative dip-slip created the accommodation space for the deposition of proximal coarse grained to finer alluvial and slope deposits coming from the dismantling of Mt. Vettore and from northern catchments of the PGC basin. The thickening of the shallow alluvial complex and the different elevations of the base of unit B across VF suggest a cumulative throw of ~80 m, resulting from incremental displacements since the late part of the Middle Pleistocene, as suggested by previous estimates (Villani, Sapia, et al., 2019). The additional splay to the East (F1b at x = 1,000 m, dashed white line in Figure 4) may be considered a synthetic splay of the basal fault of Mt. Vettore, not reported in previous works and with no evident surface expression. Although lacking an evident surface fault scarp, the electrical signature of this fault (i.e., shallow lateral resistivity changes) suggests its recent activity.

The easternmost fault plotted onto the model edge (labeled as F1a in Figure 4) is traced based on previous geological and ERT surveys (Pierantoni et al., 2013; Villani, Sapia, et al., 2019). This splay is located on the topographic break at the base of the long-term cumulative fault scarp of Mt. Vettore–Mt. Redentore (Coste del Vettore in Figure 2; Pierantoni et al., 2013). A previous high-resolution shallow ERT (<100 m deep, Villani, Sapia, et al., 2019), purposely centered on the presumed morphological expression of fault F1a, yielded a clear geophysical signature of fault activity. From this study, the recovered subvertical, moderately resistive region, was interpreted as the uppermost expression of the fault zone, coexisting with an abrupt thickening of low-resistivity fine-grained deposits (ρ <250 Ωm) in its hangingwall. Unfortunately, the fault zone F1 of Villani, Sapia, et al. (2019) corresponds to the unresolved edge of our 2-D model; nonetheless, the low-resistivity fine-grained unit can be related to the shallow unit A in the 2-D transect.

3.4. 3-D Model Results

The 3-D model of the whole survey area is shown in Figure 5. The model highlights subsurface structures with abrupt lateral and vertical resistivity variations. To describe the most significant model features, in Figure 6 we show four horizontal slices at 1,150, 1,050, 950, and 750 m a.s.l. (corresponding to average depths of 150, 250, 350, and 550 m b.g.l., respectively), complemented by four cross-sections (Figure 8). In Figure 7, we also show the distribution of the normalized global sensitivity function on the four slices (details in supporting information S5). This plot indicates that all the structural and stratigraphic features we discuss in the following are reliably resolved.

At a broad scale, we recognize four main different structural domains (Figure 6): (1) a main and wide depocenter with smooth topography and maximum depth of 550–600 m in the central and southern sectors (PGC basin South labeled in Figure 6); (2) a northern sector with a shallow top-basement (100–300 m; PGC basin North); (3) a high resistive (ρ >2,000 Ωm) limestone structural high (Mt. Guaidone) in the central part; and (4) a thin, arc-shaped low resistivity structure to the SE.

More in detail, the wide low-resistivity region (ρ <200 Ωm) in the SW portion of the area delineates the dominant electrical signature of the southern part of the PGC basin, characterized by a conductive infill. Such low resistivity values match with fine-grained deposits likely attributable to distal phases of alluvial fans alternating with fluviolacustrine deposits. The shallower portion of this structure is about 4 km long in the NNE—SSW direction and about 1.5 km wide in the WNW—ESE direction. It is bounded by high resistivity regions to the East and to the West through high-angle discontinuities that strike NNE, delineating the basin boundaries.

Just to the North of the PGC basin South, we found a sharp transition to a region of complex pattern with moderately high resistivity (around ρ ~400–500 Ωm; Figure 6c) and local conductive shallow patches (ρ <200 Ωm; Figure 8a). This region likely represents a second shallow, less developed depocenter characterized by a mixture of coarse and prevailing fine deposits (PCG basin North). Due to logistical limitations, this part of the basin was only partially investigated by our 3-D survey, therefore the existence of such a secondary depocenter is mainly aided by previous geophysical surveys of Villani, Sapia, et al. (2019). To the NE, the PGC South grades into a sector characterized by a different resistivity pattern. The latter consists of NNW-trending stripes of high and low resistivity, which we relate to the presence of NNW-trending

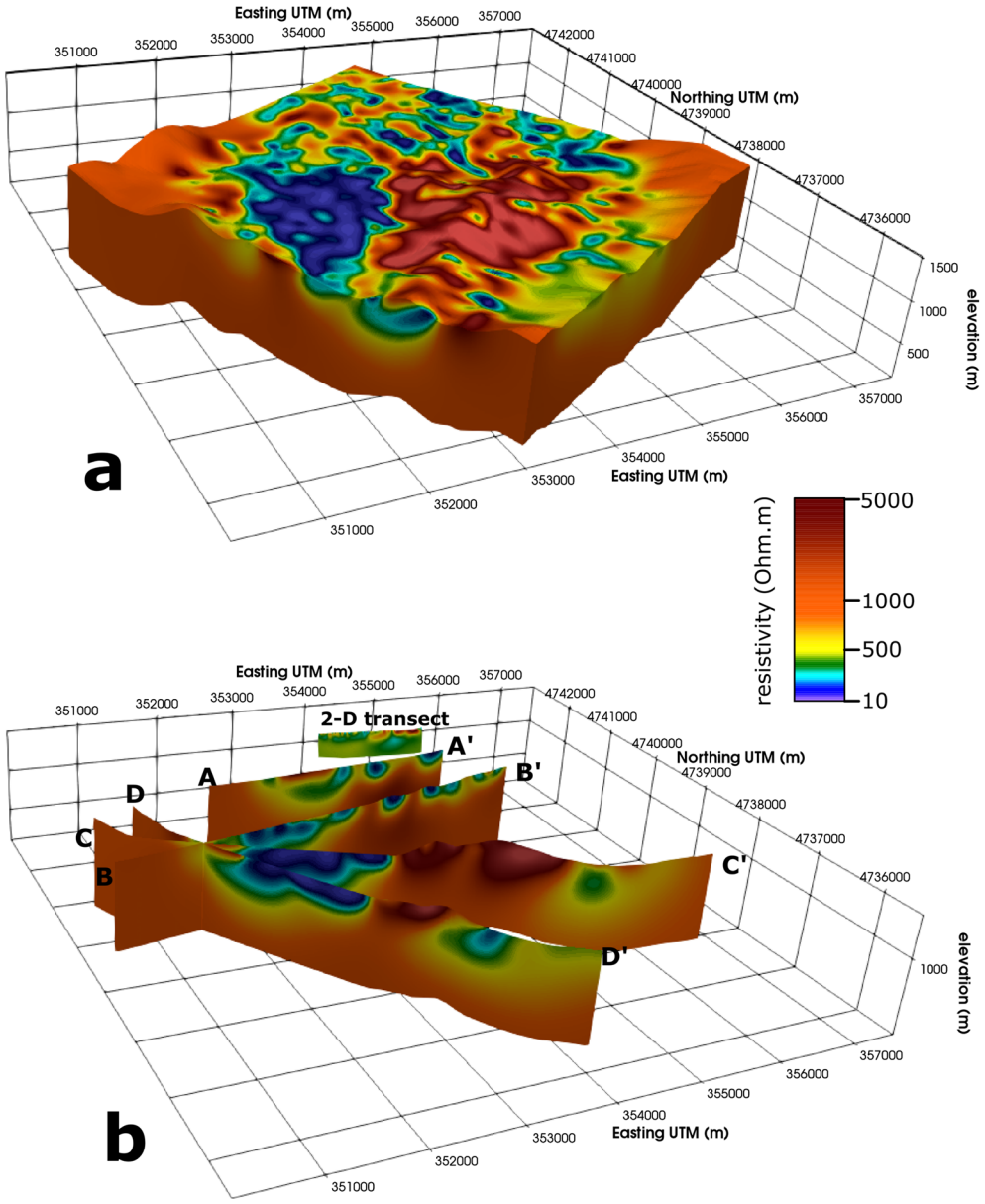

Figure 5. Results of the 3-D Fullwaver survey. (a) Perspective view of the resistivity model. UTM metrical coordinates (WGS84 datum, zone 33N). (b) Selected cross-sections of the 3-D FW resistivity model. A simplified structural interpretation of the sections is provided in Figure 8.

faults (marked with pink lines in Figures 8a and 8b). This interpretation is coherent with the results of the high-resolution 2-D transect. For instance, the main fault VF unraveled by the 2-D survey corresponds to an evident lateral resistivity variation in the 3-D model (Figures 6 and 8a).

In the SE part of the survey area, we observe a relatively low-resistivity arc-shaped region (ρ ~300–500 Ωm), about 0.5 km wide and 5-km long, visible down to a depth of 550 m. This low-resistivity structure is bounded to the West by a wide region of high-resistivity (ρ >2,000 Ωm) that corresponds to the Mt. Guaidone limestone structural high, which in turns delimits to the East of the PGC basin South. Cross-sections (Figures 8c and 8d) clearly show that the low-resistivity arc-shaped belt gently dips to the NW, below the Mt. Guaidone structural high, suggesting the presence of a NW-dipping fault, possibly a thrust as discussed later (T in Figures 6, 8c, and 8d).

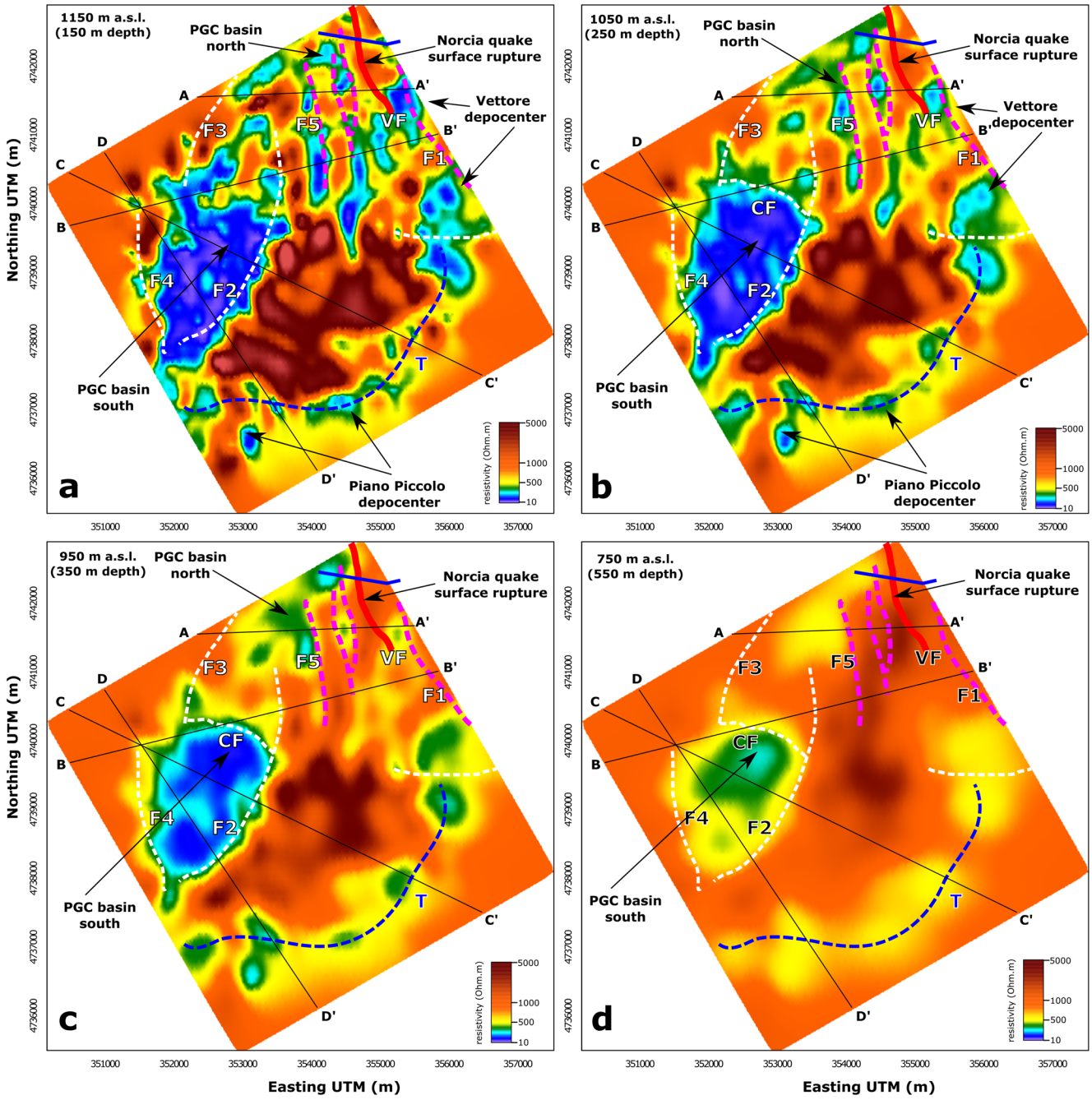

Figure 6. Horizontal slices of the 3-D Fullwaver resistivity model at 1,150 m (a), 1,050 m (b), 950 m (c), and 750 m (d) a.s.l. with simplified structural interpretation. The dashed lines (white, pink, and blue) are inferred fault zones, the 2016 surface ruptures are indicated with a *red* line (see details in the text for the meaning of the different colors), whereas the thin black lines are the traces of the cross-sections depicted in Figure 8, and the thick blue line is the trace of the 2-D transect. UTM metrical coordinates (WGS84 datum, zone 33N).

Surface geology (Figures 2, 8c and 8d; Pierantoni et al., 2013) shows two small depressions at the northern and southern edges of the arc-shaped conductive belt (Pian Piccolo and Fonte Vetica, respectively). Such depressions are characterized by a thin cover of alluvial and slope debris deposits: thus, the resistivity model confirms the presence of those two depocenters. We interpret the northern depocenter (Fonte Vetica) as a small hangingwall basin related to the southernmost part of the Mt. Vettore basal fault (F1). It is difficult to infer the thickness of those continental depocenters located along this conductive anomaly (Figure 8c).

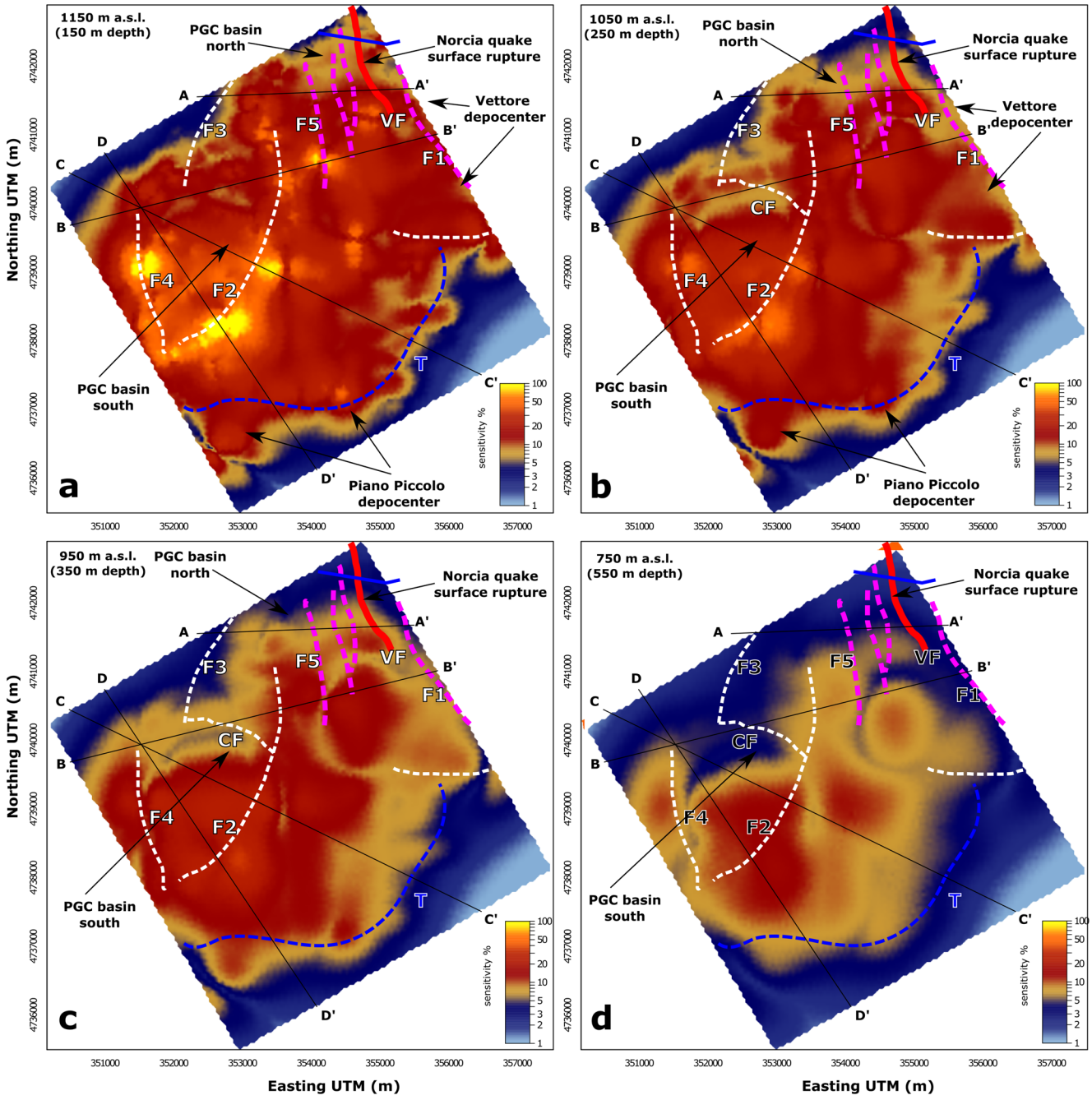

Figure 7. Horizontal slices of the normalized sensitivity function at depths of 1,150, 1,050, 950, and 750 m a.s.l. (see for comparison slices of resistivity shown in Figure 6). All the main structural and stratigraphic features discussed in this work belong to regions characterized by significant sensitivity and therefore they have to be considered reliably resolved. UTM metrical coordinates (WGS84 datum, zone 33N).

4. Discussion

4.1. Fault Systems of the PGC Basin

The first 3-D image of the PGC here presented leads to a remarkable improvement in the understanding of the subsurface architecture and tectonic evolution of the basin with respect to previously published studies (e.g., Calamita, Pizzi, & Roscioni, 1992; Villani, Sapia, et al., 2019). The main structures, mostly unknown prior to our survey, delineated by the resistivity patterns, are schematically reported in Figure 9.

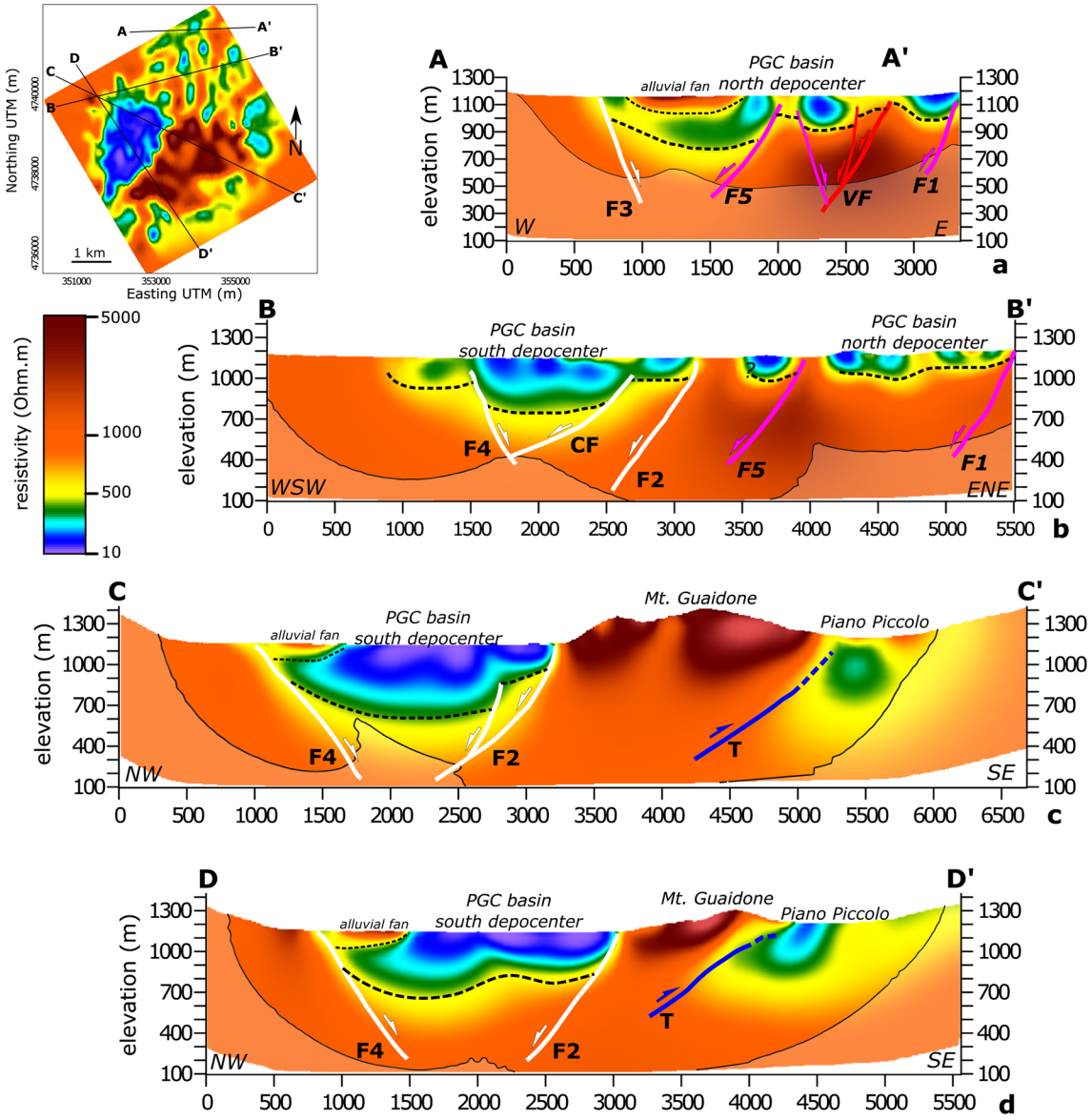

Figure 8. Cross-sections of the 3-D FW resistivity model (traces shown in the top left inset, corresponding to the slice at 1,050 m a.s.l. in Figure 6), with simplified structural interpretation. White lines indicate faults belonging to the 20°–30°N system, pink lines indicate faults of the 150°–170°N system (VBFS), whereas the blue lines indicate a possible shallow thrust splay (T) dipping to the NW. The dashed black line indicates the inferred top basement. The thin black line is the contour indicating the 3% of the normalized sensitivity function (see supporting information S5 for details). The regions with sensitivity < 3% were masked with transparency.

We interpret the main sharp lateral resistivity variations of the 3-D model as fault zones (labeled as F1, F2, F3, F4, F5, VF, and T in Figures 6 and 8) that cause vertical displacements of the limestone basement of several tens of meters. Two main fault sets (striking 20°–30°N and 150°–170°N) characterize the area, resulting in an interference pattern that produces structural complexity (Figure 6). The southern sector (i.e., PGC South) is basically controlled by two normal fault zones (F2 and F4), while in the PGC North several normal fault splays accommodate the extension. The orientation of the main fault zones is about 20°–30°N in the southern and western sectors of the study area (F2, F3, and F4), while faults strike NNW to NW in the northern part (F1, F5, and VF). We interpret these latter faults as synthetic splays of the VBFS, suggesting that the shallow structure of the fault system responsible for the 2016, M_w 6.5, Norcia earthquake exhibits branching of several second-order faults. They are organized into a wide and distributed brittle deformation zone. Based on their geophysical signature, the main faults F2, F3, and F4 are characterized by individual

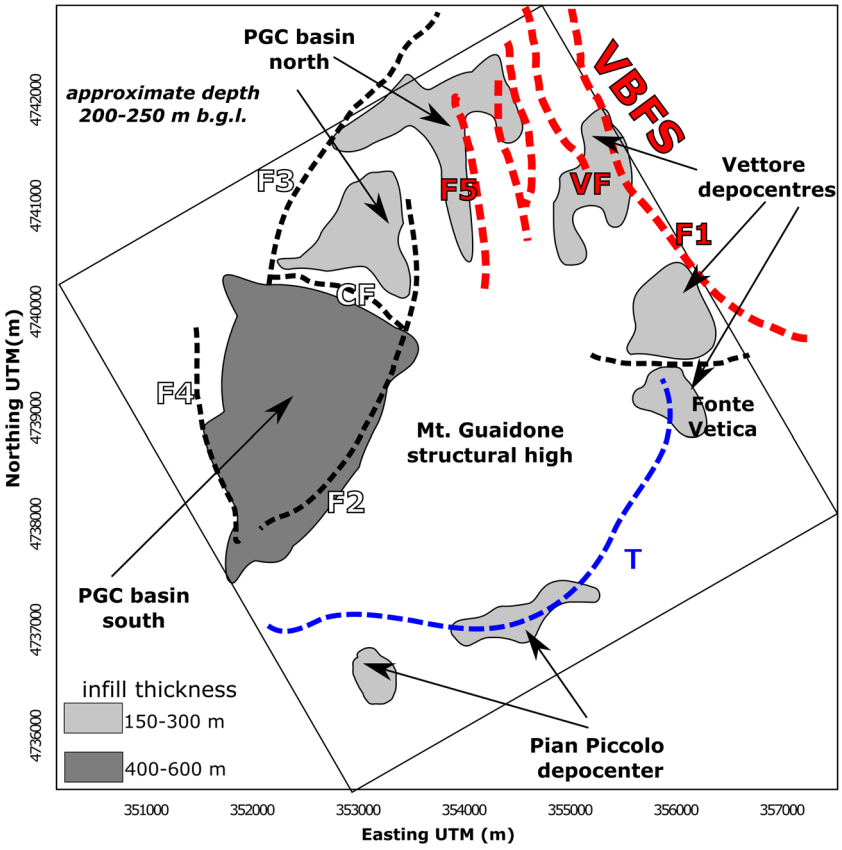

Figure 9. Sketch of the structural setting of the PGC basin area as inferred from the 3-D resistivity model. The main depocenters are colored with different shadings according to the presumed maximum thickness of the basin infill. Old and possibly inactive faults (F2, F3, F4, CF) are marked with dashed black lines, while currently active splays of the VBFS are in red. The NW-dipping blind thrust T is marked with a blue line. UTM metrical coordinates (WGS84 datum, zone 33N).

throws in the order of ~300, ~350 and ~400 m, respectively, whereas faults F1, VF, and F5 (which we consider as splays of the VBFS) are characterized by throws in the order of ~300, ~200 and ~250 m, respectively. Because such throw values refer to the displacement of electrical units (i.e., high resistivity substratum), they represent a minimum estimation of the geologic fault throws. This point arises from two main reasons: (1) the difficulty in distinguishing high resistivity and coarse clastics from the underlying limestone substratum in the faults' hangingwall; (2) the uncertain age of the limestone substratum across the fault (which from geological maps may range from lower Jurassic to upper Cretaceous) due to the lack of borehole data. For instance, it is well established that the geologic throw of the fault zone at the base of Mt. Vettore (that includes F1) largely exceeds 1,000 m (Brozzetti et al., 2019; Pizzi & Scisciani, 2000; Porreca, Fabbrizzi, et al., 2020; Villani, Sapia, et al., 2019).

The evolution of the PGC basin was likely controlled also by a WNW–ESE trending cross-fault (CF, visible from 250 m depth in Figures 6b-d). This fault zone contributes to separate the two main depocenters that coalesced to form the present-day basin.

The arc-shaped fault T (Figures 6, Figures 8c, and 8d) that gently dips NW underneath the Mt. Guaidone structural high, is incompatible with normal fault kinematics. Conversely, its position and geometry seem consistent with a blind thrust, possibly associated with an open footwall syncline. Surface geology indicates that the pre-Quaternary substratum outcropping to the East of the Mt. Guaidone structural high includes marly-clayey Jurassic formations (Pierantoni et al., 2013) laying within a NE-trending syncline, which may have developed in the footwall of the underlying blind thrust. Those marly units, together with the NW-dipping fault-zone, may be responsible for the arc-shaped and large-

scale low-resistive anomaly, which includes the small-scale conductive response of the Pian Piccolo and Fonte Vetica depocenters (Figures 6a–6c). Notably, the inferred blind thrust T parallels the regional MST, a Late Miocene-Pliocene first-order structure (Calamita, Pace, & Satolli, 2012), which outcrops few kilometers to the SE (MST in Figure 1a). The MST presents a marked curvature with a strike change just to the SE of the PGC. This bend mimics the arc-shaped resistivity anomaly related to fault T (Figure 1a). Based on these observations, we hypothesize that fault T represents a minor hangingwall splay of the MST.

4.2. Internal Structure and Evolution of the PGC Basin

A main result of our study is the identification of two distinct depocenters, with different size and structure. The northern depocenter (PGC basin North, Figure 9) is segmented by several ~NNW-trending faults and exhibits a relatively shallow basement, ~100–300 m deep. On the contrary, the southern depocenter (PGC basin South, Figure 9) is ~500–600 m deep and 2 km wide with a homogeneous low-resistivity signature. Those two depocenters are bounded by two different sets of conjugate normal faults (Figures 6 and 8). The northern depocenter is bounded by faults F1, F5, VF striking 150°–170°N. The southern one is bounded by faults F2, F3, striking 20°–30°N. In addition, we recognize two important large-displacement transverse faults (F4 and CF). The interplay of those faults gives rise to the peculiar rhomboid shape of the PGC basin, which is markedly oblique to the general NW to NNW trend of the active normal faults in the central Apennines, as the VBFS. As also revealed by our 2-D transect across the 2016 Norcia earthquake coseismic surface ruptures (Figure 4), only the splays belonging to the VBFS show consistent evidence of activity in recent times (more details in Villani, Pucci, et al., 2018). All this suggests that the geological evolution of the basin likely took place in two different tectonic phases. In the first phase, only the faults F2, F3, and F4 were mainly active, creating the southern large PGC depocenter and an additional smaller depocenter related to the activity of fault F1 located at the base of Mt. Vettore (Figure 9). In the second phase, the NNW-trending faults F1, F5, and VF likely played a major role in accommodating deformation that concurred to the generation of a segmented depocenter to the North. In particular, VF (Figure 4) is the only fault within the basin that ruptured the surface during the 2016 Norcia mainshock, and for which it has been possible to reconstruct the tectonic activity from the Middle Pleistocene to the Late Holocene thanks to paleoseismic data (Galadini & Galli, 2003; Galli, Galderisi, et al., 2019) and recent high-resolution ERT surveys (Villani & Sapia, 2017). We interpret the high resistive anomaly observed in VF footwall as due to the presence of coarse clastic deposits above the limestone substratum. The absence of an analog high resistivity patch in the VF hangingwall allows us to hypothesize that the total throw of VF is >140 m. In this scenario, the fault at the base of the Mt. Vettore (F1a in Figure 4) accrued a large portion of displacement (several hundred meters) thus concurring to the early development of the northern part of the PGC basin. Unfortunately, due to the lack of dating of the deep basin infill materials, the timing of the earlier tectonic phase remains unconstrained. However, we hypothesize that the beginning of the basin development may be, at least, as old as Early Pleistocene, since its infill thickness exceeds the known thickness of several Early-Middle Pleistocene basins in the central Apennines (Cavinato & De Celles, 1999).

It is likely that inherited compressional tectonic structures trending NNE affected the present basin geometry, and possibly played an important role in controlling the orientation of the normal faults. Indeed, they appear to rotate from the NNE-oriented normal faults bounding the main southern depocenter to the ~NNW-trending splays of the currently active VBFS.

The identification of a possible shallow thrust structure to the East of the PGC basin (fault T in Figures 6, 8 and 9), in a more internal position with respect to the MST, is a relevant result of our study that has straightforward implication on the source model of the Norcia, M_w 6.5, mainshock. We yield indeed the first geophysical image of a transverse, NW-dipping, blind fault beneath the PGC basin. This fault likely concurred to coseismic slip during the Norcia mainshock, as proposed by seismological and geodetic rupture models (Scognamiglio et al., 2018; Walters et al., 2018) and suggested by the alignment of strong early aftershocks (Improta, Latorre, et al., 2019). In this view, our study reinforces these previous interpretations, supporting a rupture scenario in which a NE-trending cross-structure, misoriented in the present extensional stress field with SH_{max} direction striking NNW, played a primary role on slip propagation and on the segmentation of the VFBS.

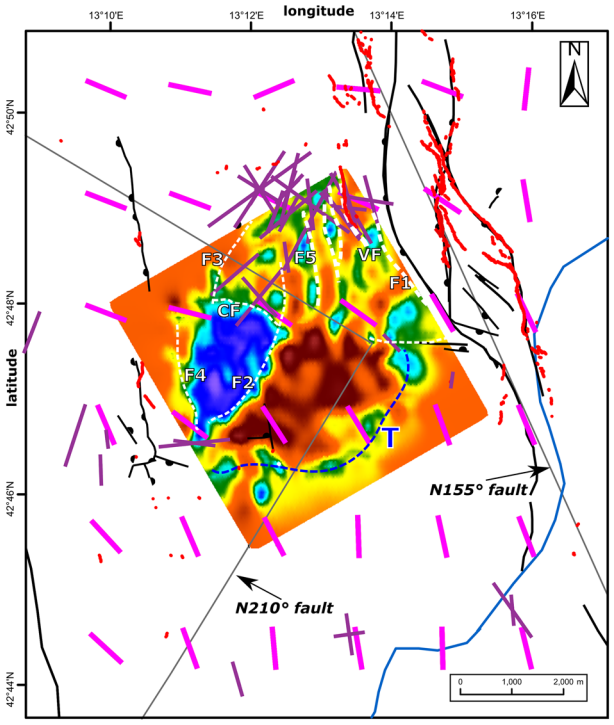

Figure 10. Relations between surface resistivity anomalies and fracture pattern inferred from crustal shear wave anisotropy. A slice of the Fullwaver model at 1,050 m a.s.l. (see Figure 6b) is compared with crustal S-wave splitting results: fast axes from Villani, Sapia, et al. (2019) are dark violet bars (length proportional to delay time), while pink bars indicate fast axes by Pastori et al. (2019) spatially averaged at regular intervals through a nearest neighbor algorithm using a search radius of 6 km, smoothing factor $\lambda = 1$, and output grid size of 0.04° (in this case, bar length is not scaled to delay time). Geographic coordinates, WGS84 reference datum, zone 33N.

The complex fault architecture in the Castelluccio area with differently oriented sets of faults fits previous interpretation of S-wave splitting measurements, in which different trends of crustal S-wave fast directions have been interpreted in terms of combined stress-induced and structurally controlled anisotropy (Figure 10; Pastori et al., 2019; Villani, Sapia, et al., 2019). In particular, the occurrence of NNW- and NE-trending faults in the northern part of the basin (F1, F3, F5, VF in Figures 6 and 8) reconciles with results obtained by Villani, Sapia, et al. (2019) using local temporary stations installed within the basin. The large-scale compartmentalization of this depression in two main depocenters guided by a deep and nearly WNW-ESE trending fault system (CF), is supported by the dominant trend of averaged fast directions obtained by Pastori et al. (2019) through the analysis of thousands of aftershock data of the 2016–2017 sequence recorded in the hangingwall of the VBFS by permanent stations. Notably, the inferred shallow arcuate thrust splay T is laterally confined by two belts of dominant WNW—ESE trending fast axes, particularly in correspondence of the southern tip (Figure 10).

Additionally, we can infer on the physical properties of the deep carbonate sequences in the VBFS hangingwall. The array of blind faults imaged in the northern part of the PGC basin, points to an intense fracturing of the hangingwall block. This could explain two peculiarities of the 2016–2017 seismic sequence: (i) the diffuse aftershock activity and lack of aftershock alignments observed by Chiaraluce et al. (2017) and Improta, Latorre, et al. (2019) in the upper 4 km of the crust under the basin and (ii) the NW-migration of the off-fault aftershocks of the 24 August M_w 6.0 Amatrice earthquake, as well as the triggering of the 26 October Visso and 30 October Norcia mainshocks, modeled invoking pore-fluid diffusion along NW-trending fault zones (Convertito et al., 2020; Tung & Masterlark, 2018; Walters et al., 2018).

According to the available geological and geophysical data for the area, the PGC basin shares various traits with other extensional basins in the Apennines. In the Middle Aterno basin (2009 M_w 6.1 L'Aquila earthquake area) the early depocenters were controlled during the Early Pleistocene by W- and NNE-trending inherited faults that subsequently linked with NW-trending faults that are now active and seismogenic (Civico, Sapia, et al., 2017; Pucci, Villani, et al., 2019). Older CFs trending NE and reactivated in recent times characterize the large Fucino basin, bounded by NW-trending seismogenic normal faults (M_w 6.9 1915 earthquake; Cavinato et al., 2002). In the Val d'Agri basin (southern Apennines), Early-Middle Pleistocene strike-slip along NW-trending faults bounding the eastern margin (Colella et al., 2004) was followed by extension promoted by NE-dipping normal faults on the western side and that represent the main seismogenic sources (Improta, Ferranti, et al., 2010; Maschio et al., 2005).

These common features confirm that crustal geometric and rheological heterogeneities inherited from paleogeographic discontinuities and/or previous tectonic phases play a crucial role in the evolution of extensional basins within relatively young thrust belts like the Apennines.

From a methodological point of view, our study illustrates the effectiveness of the FW technology to image the 3-D structure of complex basins. Higher-resolution images can be obtained using a denser acquisition/source geometry. This point is critical to obtain accurate information on the different sedimentary sequences filling complex intramontane basins.

5. Conclusions

By using an FW technology with a multiscale 2-D/3-D imaging strategy, we investigated the PGC basin infill and its buried geometry down to a depth of ~1 km. This was the first time that such a geophysical tool targeted a large basin related to a main seismogenic fault system. Our results document that the adopted geophysical approach turned as an effective strategy to provide a reliable 3-D image of the basin geometry and to detect a complex system of faults. The latter was mostly unknown prior to our survey. With regard to the 2-D high-resolution transect, we imaged the subsurface picture of the M_w 6.5 2016 earthquake ruptures and we identified additional conjugate blind splays. Concerning the large-scale 3-D model, we imaged two distinct depocenters with different depths, controlled by two sets of conjugate normal faults trending 20°–30°N and 150°–170°N, respectively. We interpreted those different fault systems as the result of a polyphase tectonic evolution, likely spanning the whole Quaternary. Moreover, the 3-D model points to the presence of a shallow blind thrust splay, which may correspond to a subsidiary NE-dipping splay of the MST thrust invoked by recent multi-segment rupture models of the complex 2016 Norcia earthquake.

Overall, the obtained results enabled us to depict the PGC basin as due to the long-term evolution of a complex fault system interacting with inherited structures and which became part of a major seismogenic fault responsible for large, destructive earthquakes.

Data Availability Statement

Data supporting the conclusions can be found in the cited references and at the following link: https://doi.org/10.6084/m9.figshare.14191319.

Acknowledgments
The survey has been carried out in the framework of the Project INGV MIUR-FISR 2016–2017 "4-D Structure of central Italy and active geodynamics process: Task 1–3-D Structure of Central Italy" (Task leader L. Improta). We thank Dr. Carlo Bifulco (president of the Mt. Sibillini National Park), Nicola Alemanno (mayor of Norcia), and the Carabinieri Forestali of Visso that provided the authorizations to perform the geophysical survey in the Castelluccio basin. We also thank Giulia Penno and Filippo Barsuglia from Geostudi Astier srl (Livorno, Italy) for technical support in the field during the geophysical campaign. We warmly acknowledge M. Gresse and an anonymous reviewer for their constructive comments, which helped us improve the quality of the manuscript.

References

Balasco, M., Galli, P., Giocoli, A., Gueguen, E., Lapenna, V., Perrone, A., et al. (2011). Deep geophysical electromagnetic section across the middle Aterno Valley (central Italy): Preliminary results after the April 6, 2009 L'Aquila earthquake. *Bollettino di Geofisica Teorica ed Applicata*, *52*(3), 443–455. https://doi.org/10.4430/bgta0028

Barker, R. D. (1991). Depth of investigation of collinear symmetrical four-electrode arrays. *Geophysics*, *54*, 1031–1037. https://doi.org/10.1190/1.1442728

Boncio, P., & Lavecchia, G. (2000). A structural model for active extension in central Italy. *Journal of Geodynamics*, *29*(3-5), 233–244. https://doi.org/10.1016/S0264-3707(99)00050-2

Boncio, P., Lavecchia, G., & Pace, B. (2004). Defining a model of 3-D seismogenic sources for seismic hazard assessment applications: The case of central Apennines (Italy). *Journal of Seismology*, *8*, 407–425. https://doi.org/10.1023/B:JOSE.0000038449.78801.05

Brozzetti, F., Boncio, P., Cirillo, D., Ferrarini, F., Nardis, R., Testa, A., et al. (2019). High-resolution field mapping and analysis of the August-October 2016 coseismic surface faulting (central Italy earthquakes): Slip distribution, parameterization, and comparison with global earthquakes. *Tectonics*, *38*(2), 417–439. https://doi.org/10.1029/2018TC005305

Burbank, D. W., & Anderson, R. S. (2011). *Tectonic geomorphology*. Wiley-Blackwell.

Butler, D. K. (2005). Near-surface geophysics. *Society of Exploration Geophysicists*, *13*, https://doi.org/10.1190/1.9781560801719

Calamita, F., Pace, P., & Satolli, S. (2012). Coexistence of fault-propagation and fault-bend folding in curve-shaped foreland fold-and-thrust belts: Examples from the Northern Apennines (Italy). *Terra Nova*, *24*(5), 396–406. https://doi.org/10.1111/j.1365-3121.2012.01079.x

Calamita, F., Pizzi, A., & Roscioni, M. (1992). I fasci di faglie recenti ed attive di M. Vettore—M. Bove e di M. Castello – M. Cardosa (appennino Umbro-Marchigiano). *Studi Geologici Camerti*, *1992*(1), 81–95. http://doi.org/10.15165/studgeocam-1198

Carrier, A., Fischanger, F., Gance, J., Cocchiararo, G., Morelli, G., & Lupi, M. (2019). Deep electrical resistivity tomography for the prospection of low- to medium-enthalpy geothermal resources. *Geophysical Journal International*, *219*(3), 2056–2072. https://doi.org/10.1093/gji/ggz411

Cavinato, G. P., Carusi, C., Dall'Asta, M., Miccadei, E., & Piacentini, T. (2002). Sedimentary and tectonic evolution of Plio-Pleistocene alluvial and lacustrine deposits of Fucino Basin (central Italy). *Sedimentary Geology*, *148*(1), 29–59. http://doi.org/10.1016/S0037-0738(01)00209-3

Cavinato, G. P., & De Celles, P. G. (1999). Extensional basins in the tectonically bimodal central Apennines fold-thrust belt, Italy: Response to corner flow above a subducting slab in retrograde motion. *Geology*, *27*(10), 955–958. https://doi.org/10.1130/0091-7613(1999)027%3C0955:EBITTB%3E2.3.CO

Chiarabba, C., Jovane, L., & DiStefano, R. (2005). A new view of Italian seismicity using 20 years of instrumental recordings. *Tectonophysics*, *395*, 251–268. https://doi.org/10.1016/j.tecto.2004.09.013

Chiaraluce, L., DiStefano, R., Tinti, E., Scognamiglio, L., Michele, M., Casarotti, E., et al. (2017). The 2016 Central Italy seismic sequence: A first look at the mainshocks, aftershocks, and source models. *Seismological Research Letters*, *88*(3), 757–771. https://doi.org/10.1785/0220160221

Cinti, F. R., De Martini, P. M., Pantosti, D., Baize, S., Smedile, A., Villani, F., et al. (2019). 22-kyr-Long record of surface faulting along the source of the 30 October 2016 earthquake (Central Apennines, Italy), from integrated paleoseismic data sets. *Journal of Geophysical Research: Solid Earth*, *124*, 8. https://doi.org/10.1029/2019JB017757

Civico, R., Pucci, S., Villani, F., Pizzimenti, L., De Martini,P. M., Nappi, R., & The Open EMERGEO Working Group (2018). Surface ruptures following the 30 October 2016 Mw 6.5 Norcia earthquake, central Italy. *Journal of Maps*, *14*(2), 151–160. https://doi.org/10.1080/17445647.2018.1441756

Civico, R., Sapia, V., Di Giulio, G., Villani, F., Pucci, S., Baccheschi, P., et al. (2017). Geometry and evolution of a fault-controlled quaternary basin by means of TDEM and single-station ambient vibration surveys: The example of the 2009 L'Aquila earthquake area. *Journal of Geophysical Research: Solid Earth*, *122*, 2236–2259. https://doi.org/10.1002/2016JB013451

Colella, A., Lapenna, V., & Rizzo, E. (2004). High-resolution imaging of the High Agri Valley Basin (Southern Italy) with electrical resistivity tomography. *Tectonophysics*, *386*, 29–40. https://doi.org/10.1016/j.tecto.2004.03.017

Coltorti, M., & Farabollini, P. (1995). Quaternary evolution of the Castelluccio di Norcia Basin, Il Quaternario. *Italian Journal of Quaternary Sciences*, *8*, 149–166.

Convertito, V., De Matteis, R., Improta, L. & Pino, N. A. (2020). Fluid-triggered aftershocks in an anisotropic hydraulic conductivity geological complex: The case of the 2016 Amatrice sequence, Italy, *Frontiers of Earth Science*, *8*, 541323. https://doi.org/10.3389/feart.2020.541323

Cowie, P. A., Phillips, R. J., Roberts, G. P., McCaffrey, K., Zijerveld, L. J. J., Gregory, L. C., et al. (2017). Orogen-scale uplift in the central Italian Apennines drives episodic behaviour of earthquake faults, *Scientific Reports*, *7*, 44858. https://doi.org/10.1038/srep44858

Cowie, P. A., & Roberts, G. P. (2001). Constraining slip rates and spacings for active normal faults. *Journal of Structural Geology*, *23*, 1901–1915. https://doi.org/10.1016/S0191-8141(01)00036-0

Everett, M. E. (2013). *Near-surface applied geophysics*. Cambridge University Press.

Galadini, F., & Galli, P. (2000). Active tectonics in the central Apennines (Italy)—Input data for seismic hazard assessment. *Natural Hazards*, *22*(3), 225–268. https://doi.org/10.1023/a:1008149531980

Galadini, F., & Galli, P. (2003). Paleoseismology of silent faults in the Central Apennines (Italy): The Mt. Vettore and Laga Mts. faults. *Annals of Geophysics*, *46*(5), 815–836. https://doi.org/10.4401/ag-3457

Galli, P., Galadini, F., & Pantosti, D. (2008). Twenty years of paleoseismology in Italy. *Earth-Science Reviews*, *88*(1), 89–117. https://doi.org/10.1016/j.earscirev.2008.01.001

Galli, P., Galderisi, A., Peronace, E., Giaccio, B., Hajdas, I., Messina, P., et al. (2019). The awakening of the dormant Mount Vettore fault (2016 central Italy earthquake, Mw 6.6): Paleoseismic clues on its millennial silences. *Tectonics*, *38*, 687–705. https://doi.org/10.1029/2018TC005326

Gance, J., Leite, O., Texier, B., Bernard, J., & Truert, C. (2018). The Fullwaver systems: Distributed network of autonomous devices for deep 3-D electrical resistivity and induced polarization survey. In EGU General Assembly Conference Abstracts EGU General Assembly Conference Abstracts.

Gawthorpe, R. L., & Leeder, M. R. (2000). Tectono-sedimentary evolution of active extensional basins. *Basin Research*, *12*, 195–218. https://doi.org/10.1111/j.1365-2117.2000.00121.x

Geomineraria Nazionale (1963). Il bacino di Castelluccio di Norcia, In *Ligniti e Torbe dell'Italia continentale (pp. 207–210)*. Torino: Industria Libraria Tipografica Editrice (ILTE).

Giocoli, A., Galli, P., Giaccio, B., Lapenna, V., Messina, P., Peronace, E., et al. (2011). Electrical resistivity tomography across the Paganica-San Demetrio fault system (L'Aquila 2009 earthquake). *Bollettino Geofisica Teorica e Applicata*, *52(3)*, 457–469. https://doi.org/10.4430/bgta0029

Haining, R. P., Kerry, R.,& Oliver, M. A. (2010). Geography, spatial data analysis, and geostatistics: An overview. *Geographical Analysis*, *42*, 7–31. https://doi.org/10.1111/j.1538-4632.2009.00780.x

Improta, L., Ferranti, L., De Martini, P. M., Piscitelli, S., Bruno, P. P., Burrato, P., et al. (2010). Detecting young, slow-slipping active faults by geologic and multidisciplinary high-resolution geophysical investigations: A case study from the Apennine seismic belt, Italy. *Journal of Geophysical Research: Solid Earth*, *115*, B11307. https://doi.org/10.1029/2010JB000871

Improta, L., Latorre, D., Margheriti, L., Nardi, A., Marchetti, A., Lombardi, A. M., et al., & Bollettino Sismico Working Group (2019). Multi-segment rupture of the 2016 Amatrice-Visso-Norcia seismic sequence (central Italy) constrained by the first high-quality catalog of Early Aftershocks. *Scientific Reports*, *9*, 6921. https://doi.org/10.1038/s41598-019-43393-2

Lajaunie, M., Gance, J., Nevers, P., Malet, J. P., Bertrand, C., Garin, T., & Ferhat, G. (2019). Structure of the Séchilienne unstable slope from large-scale three-dimensional electrical tomography using a resistivity distributed automated system (R-DAS). *Geophysical Journal International*, *219*(1), 129–147. https://doi.org/10.1093/gji/ggz259

Lavecchia, G., Brozzetti, F., Barchi, M., Menichetti, M., & Keller, J. V. A. (1994). Seismotectonic zoning in east-central Italy deduced from an analysis of the Neogene to present deformations and related stress fields. *The Geological Society of America Bulletin*, *106*, 1107–1120. https://doi.org/10.1130/0016-7606(1994)106<1107:SZIECI>2.3.CO

Maschio, L., Ferranti, L., & Burrato, P. (2005). Active extension in Val d'Agri area, Southern Apennines, Italy: Implications for the geometry of the seismogenic belt. *Geophysical Journal International*, *162*(2), 591–609. https://doi.org/10.1111/j.1365-246X.2005.02597.x

Meghraoui, M., Camelbeeck, T., Vanneste, K., Brondeel, M., & Jongmans, D. (2000). Active faulting and paleoseismology along the Bree fault, lower Rhine graben, Belgium. *Journal of Geophysical Research: Solid Earth*, *105*(B6), 13809–13841. https://doi.org/10.1029/1999JB900236

Michele, M., Chiaraluce, L., Di Stefano, R., & Waldhauser, F. (2020). Fine-scale structure of the 2016–2017 Central Italy seismic sequence from data recorded at the Italian National Network. *Journal of Geophysical Research: Solid Earth*, *125*, e2019JB018440. https://doi.org/10.1029/2019JB018440

Okpoli, C. C. (2013). Sensitivity and resolution capacity of electrode configurations. *International Journal of Geophysics*, *2013*. https://doi.org/10.1155/2013/608037

Pastori, M., Baccheschi, P., & Margheriti, L. (2019). Shear wave splitting evidence and relations with stress field and major faults from the Amatrice-Visso-Norcia seismic sequence. *Tectonics*, *38*(9), 3351–3372. https://doi.org/10.1029/2018TC005478

Paul, J. D. (2015). High-resolution geological maps of central London, UK: Comparisons with the London Underground. *Geoscience Frontiers*, *7*(2), 273–286. https://doi.org/10.1016/j.gsf.2015.05.004

Pierantoni, P. P., Deiana, G., & Galdenzi, S. (2013). Geological map of the Sibillini Mountains (Umbria-Marche Apennines, Italy). *Italian Journal of Geosciences*, *132*(3), 497–520. https://doi.org/10.3301/IJG.2013.08

Pizzi, A., Di Domenica, A., Gallovič, F., Luzi, L., & Puglia, R. (2017). Fault segmentation as constraint to the occurrence of the main shocks of the 2016 Central Italy seismic sequence. *Tectonics*, *36*(11), 2370–2387. http://doi.org/10.1002/2017TC004652

Pizzi, A., & Scisciani, V. (2000). Methods for determining the Pleistocene–Holocene component of displacement on active faults reactivating pre-Quaternary structures: Examples from the Central Apennines (Italy). *Journal of Geodynamics*, *29*(3–5), 445–457. https://doi.org/10.1016/S0264-3707(99)00053-8

Porreca, M., Fabbrizzi, A., Azzaro, S., Pucci, S., Del Rio, L., Pierantoni, P. P., et al. (2020). 3-D geological reconstruction of the M. Vettore seismogenic fault system (Central Apennines, Italy): Cross-cutting relationship with the M. Sibillini thrust. *Journal of Structural Geology*, *131*, 103938. https://doi.org/10.1016/j.jsg.2019.103938

Porreca, M., Minelli, G., Ercoli, M., Brobia, A., Mancinelli, P., Cruciani, F., et al. (2018). Seismic reflection profiles and subsurface geology of the area interested by the 2016–2017 earthquake sequence (Central Italy). *Tectonics*, *37*, 1116–1137. https://doi.org/10.1002/2017TC004915

Pucci, S., Civico, R., Villani, F., Ricci, T., Delcher, E., Finizola, A., et al. (2016). Deep electrical resistivity tomography along the tectonically active Middle Aterno valley (2009 L'Aquila earthquake area (central Italy). *Geophysical Journal International*, *207*(2), 967–982. https://doi.org/10.1093/gji/ggw308

Pucci, S., Villani, F., Civico, R., Di Naccio, D., Porreca, M., Benedetti, L., et al. (2019). Complexity of the 2009 L'Aquila earthquake causative fault system (Abruzzi Apennines, Italy) and effects on the Middle Aterno Quaternary basin arrangement. *Quaternary Science Reviews*, *213*, 30–66. https://doi.org/10.1016/j.quascirev.2019.04.014

Pugin, A. J. M., Oldenborger, G. A., Cummings, D. I., Russell, H. A. J., & Sharpe, D. R. (2014). Architecture of buried valleys in glaciated Canadian Prairie regions based on high resolution geophysical data. *Quaternary Science Reviews*, *86*, 13–23. https://doi.org/10.1016/j.quascirev.2013.12.007

Reeve, M. T., Bell, R. E., Duffy, O. B., Jackson, C. A. L., & Sansom, E. (2015). The growth of non-colinear normal fault systems; What can we learn from 3D seismic reflection data? *Journal of Structural Geology*, *70*, 141–155. http://doi.org/10.1016/j.jsg.2014.11.007

Sapia, V., Oldenborger, G. A., Jørgensen, F., Pugin, A. J. M., Marchetti, M., & Viezzoli, A. (2015). 3-D Modeling of buried valley geology using airborne electromagnetic data. *Interpretation*, *3*(4), SAC9–SAC22. https://doi.org/10.1190/INT-2015-0083.1

Sapia, V., Viezzoli, A., Jørgensen, F., Oldenborger, G. A., & Marchetti, M. (2014). The impact on geological and hydrogeological mapping results of moving from ground to airborne TEM. *Journal of Environmental and Engineering Geophysics*, *19*(1), 53–66. https://doi.org/10.2113/jeeg19.1.53

Sapia, V., Viezzoli, A., Menghini, A., Marchetti, M., & Chiappini, M. (2015). The Italian reference site for TEM methods. *Annals of Geophysics*, *58*(5, G0548). https://doi.org/10.4401/ag-6805

Schamper, C., Jørgensen, F., Auken, E., & Effersø, F. (2014). Assessment of near-surface mapping capabilities by airborne transient electromagnetic data: An extensive comparison to conventional borehole data. *Geophysics*, *79*(4), B187–B199. https://doi.org/10.1190/geo2013-0256.1

Scognamiglio, L., Tinti, E., Casarotti, E., Pucci, S., Villani, F., Cocco, M., et al. (2018). Complex fault geometry and rupture dynamics of the M_w 6.5, 2016, October 30th central Italy earthquake. *Journal of Geophysical Research: Solid Earth*, *123*(4), 2943–2964. https://doi.org/10.1002/2018JB015603

Tarquini, S., Vinci, S., Favalli, M., Doumaz, F., Fornaciai, A., & Nannipieri, L. (2012). Release of a 10-m-resolution DEM for the Italian territory: Comparison with global-coverage DEMs and anaglyph-mode exploration via the web. *Computers and Geosciences*, *38* (1), 168–170. https://doi.org/10.1016/j.cageo.2011.04.018

Telford, W., Geldart, L., & Sheriff, R. (1990). *Applied geophysics*. Cambridge University Press. https://doi.org/10.1017/CBO9781139167932

Tondi, E. (2000). Geological analysis and seismic hazard in the Central Apennines (Italy). *Journal of Geodynamics*, *29*(3–5), 517–533. https://doi.org/10.1016/S0264-3707(99)00048-4

Troiano, A., Isaia, R., Di Giuseppe, M. G., Tramparulo, F. D. A., & Vitale, S. (2019). Deep electrical resistivity tomography for a 3-D picture of the most active sector of Campi Flegrei caldera. *Scientific Reports*, *9*(1), 1–10. https://doi.org/10.1038/s41598-019-51568-0

Tung, S., & Masterlark, T. (2018). Delayed poroelastic triggering of the 2016 October Visso earthquake by the August Amatrice earthquake, Italy. *Geophysical Research Letters*, *45*, 2221–2229. https://doi.org/10.1002/2017GL076453

Viezzoli, A., Jørgensen, F., & Sørensen, C. (2012). Flawed processing of airborne EM data affecting hydrogeological interpretation. *Ground Water*, *51*, 191–202. https://doi.org/10.1111/j.1745-6584.2012.00958.x

Villani, F., Pucci, S., Civico, R., De Martini, P. M., Cinti, F. R., & Pantosti, D. (2018). Surface faulting of the 30 October 2016 Mw 6.5 central Italy earthquake: Detailed analysis of a complex coseismic rupture. *Tectonics*, *37*(10), 3378–3410. https://doi.org/10.1029/2018TC005175

Villani, F., & Sapia, V. (2017). The shallow structure of a surface-rupturing fault in unconsolidated deposits from multi-scale electrical resistivity data: The 30 October 2016 Mw 6.5 central Italy earthquake case study. *Tectonophysics*, *717*(16), 628–644. https://doi.org/10.1016/j.tecto.2017.08.00

Villani, F., Sapia, V., Baccheschi, P., Civico, R., Di Giulio, G., Vassallo, M., et al. (2019). Geometry and structure of a fault-bounded extensional basin by integrating geophysical surveys and seismic anisotropy across the 30 October 2016 Mw 6.5 earthquake fault (central Italy): The Pian Grande di Castelluccio basin. *Tectonics*, *38*(1), 26–48. https://doi.org/10.1029/2018TC005205

Villani, F., Tulliani, V., Sapia, V., Fierro, E., Civico, R., & Pantosti, D. (2015). Shallow subsurface imaging of the piano di Pezza active normal fault (Central Italy) by high-resolution refraction and electrical resistivity tomography coupled with time-domain electromagnetic data. *Geophysical Journal International*, *203*(3), 1482–1494. https://doi.org/10.1093/gji/ggv399

Walters, R. J., Gregory, L. C., Wedmore, L. N. J., Craig, T. J., McCaffrey, K., Wilkinson, M., et al. (2018). Dual control of fault intersections on stop-start rupture in the 2016 Central Italy seismic sequence. *Earth and Planetary Science Letters*, *500*, 1–14. https://doi.org/10.1016/j.epsl.2018.07.043

Yilmaz, O. (2001). Seismic data analysis, (2 volumes), society of exploration geophysicists. *SEG Investigations in Geophysics*, *10*, 1000.